

Three-dimensional shape analysis from an image sequence of projected fringes and Continuous Wavelet Transform

Jesús Villa^{a,*}, Gamaliel Moreno^a, Gustavo Rodríguez^a, Ismael de la Rosa^a,
Rumen Ivanov^b, Jorge Luis Flores^c, Daniel Alainz^a

^a*Unidad Académica de Ingeniería Eléctrica, Universidad Autónoma de Zacatecas, Av. Ramón López Velarde 801, Zacatecas 98000, México*

^b*Unidad Académica de Física, Universidad Autónoma de Zacatecas, Calz. Solidaridad, Esquina Paseo de la Bufo s/n, Zacatecas 98060, México.*

^c*Departamento de Electrónica, Universidad de Guadalajara, Av. Revolución 1500, C.P. 44840 Guadalajara, Jalisco, México*

Abstract

We present in this paper a method for depth recovery that uses an image sequence of projected fringes on to the target object. The use of the Continuous Wavelet Transform (CWT) for analyzing the sinusoidal variation intensity along the image sequence at each pixel (in only one-dimension) permits the recovery of the object's depth, avoiding the inherent complexity of spatial two-dimensional processing, specially the two-dimensional phase unwrapping. We present some simulated and real experiments that validates the proposal.

Keywords: Shape analysis, Wavelets, Profilometry

2010 MSC: 00-01, 99-00

1. Introduction

In the field of computer vision, profilometry for the measurement of three-dimensional objects based on fringe projection is a well-known technique [1, 2, 3, 4, 5, 6, 7]. The basic idea of profilometry is the projection of fringes over the measured object. This is an easy and efficient way to characterize three-

*Corresponding author

Email address: jvillah@uaz.edu.mx (Jesús Villa)

dimensional information because the image of the grating is phase-modulated according to the 3-D shape of the object. The 2-D pattern image that carries the 3-D information of the object is captured and then the 3-D information is computed by means of a phase demodulation process. The great disadvantage of classical phase demodulation methodologies, which uses one or four fringe images at most, mainly represented by the Fourier methods [8, 9] and phase-shifting [10, 11, 12], respectively, is that they provide the 2-D phase wrapped. Then to recover the real dimensions of the object a 2-D phase unwrapping must be performed. As it is well known, many times 2-D phase unwrapping is a very difficult task that could become the 3-D measurement impractical. Also, when Fourier based methods are applied errors may be easily propagated, specially with the presence of discontinuities in the measured object. Due to the above mentioned problems of classical phase measuring methods in profilometry, in the last two decades there has been an increase in the research activities to develop the usually called temporal techniques which use series of fringe images changing the fringe pitch. In this kind of methods the phase computation is performed only in one dimension at every image pixel.

2. Materials and methods

2.1. Generation of an image sequence of projected fringes for depth recovery

According to Figure (1), it is well known that the intensity image model of projected fringes on to an object for depth recovery, can be approximated with the following mathematical expression:

$$g(x, y) = g_0(x, y) + g_1(x, y) \cos\{2\pi f[Z(x, y) + x] \cos \theta\}, \quad (1)$$

where $g_0(x, y)$ and $g_1(x, y)$ represent the background illumination and the amplitude modulation of intensity respectively. The fringe frequency is represented by f and the object's depth by $Z(x, y)$. The symbol θ represents the angle between the optical axes of the projector and the camera. It is known that the factor $f \cos \theta$ represents the fringe carrier frequency.

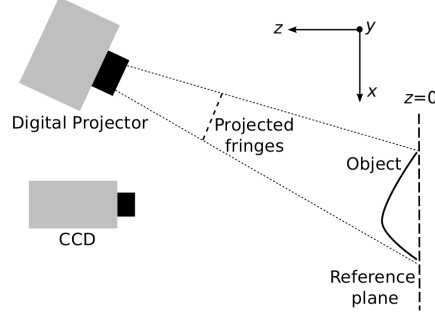


Figure 1: Schematic diagram of a basic system for object's depth measurement based on fringe projection. The projected fringes and y -axis are perpendicular to the plane of the figure.

33 The use of two-dimensional spatial or frequency methods to recover the depth
 34 $Z(x, y)$ from an image represented in (1), such as the classical work reported
 35 by Takeda *et al.* [8] and several improvements and variations of it have been
 36 widely adopted as typical tools for this purpose. Unfortunately,... We can
 37 rewrite equation (1) in terms of the system's sensibility $\varepsilon = 2\pi f \cos \theta$, that is

$$g(x, y) = g_0(x, y) + g_1(x, y) \cos\{\varepsilon[Z(x, y) + x]\}. \quad (2)$$

38 Now, it is assumed that a sequence of N fringe images are produced varying
 39 the sensibility ε , fixing θ and varying f linearly, such that

$$\varepsilon(k) = \varepsilon_1 + \mu(k - 1), \quad k = 1, 2, \dots, N. \quad (3)$$

40 To simplify the analysis the spatial dependence in (2) can be omitted, such
 41 that we can rewrite it as

$$g(k) = g_0(k) + g_1(k) \cos\{\alpha + \beta(k - 1)\}, \quad (4)$$

42 where $\alpha = \varepsilon_1[Z + x]$ and $\beta = \mu[Z + x]$.

43 As can be seen, assuming that $g_0(k)$ and $g_1(k)$ are almost constant, for a fixed
 44 point (x, y) the intensity variation along k represents a cosine function of fre-
 45 quency β . In this way, if β is estimated, Z can be computed at the point (x, y)

46 by means of

$$Z = \frac{\beta}{\mu} - x. \quad (5)$$

47 To determine the value of experimental parameters for a proper sampling of
 48 $g(k)$, we will follow the methodology described in [Quiroga] applied in deflec-
 49 tometry.

50 We can see in (4) that the phase is $\phi(k) = \alpha + \beta(k-1)$. Also, as $\phi(k)$ is a linear
 51 function, the phase difference between two consecutive samples is given by

$$\Delta\phi = \beta = \mu[Z + x]. \quad (6)$$

52 As known, for a proper sampling of (4) it is necessary to comply the Nyquist
 53 theorem, that is

$$\Delta\phi \leq \pi. \quad (7)$$

54 Given that it is possible to know the interval of Z for a given measurement,
 55 that is Z_{max} and Z_{min} , we just have to estimate μ and x , for a proper interval
 56 $[\Delta\phi_{min}, \Delta\phi_{max}]$ previously defined.

57 Considering that the vision field along x axis is determined by the interval
 58 $[x_0, x_0 + \Delta x]$, from equation (6) we can deduce that

$$\begin{aligned} \Delta\phi_{max} &= \mu[Z_{max} + x_0 + \Delta x], \\ \Delta\phi_{min} &= \mu[Z_{min} + x_0]. \end{aligned} \quad (8)$$

59 Therefore, solving this linear system for μ and x_0 , we have

$$\begin{aligned} \mu &= \frac{\Delta\phi_{max} - \Delta\phi_{min}}{Z_{max} - Z_{min} + \Delta x}, \\ x_0 &= \frac{\Delta\phi_{min}}{\mu} - Z_{min}. \end{aligned} \quad (9)$$

60 It is important to remark that estimation of a proper value of x_0 is necessary
 61 to ensure that $\beta = \mu[Z + x] > 0 \quad \forall \quad Z$.

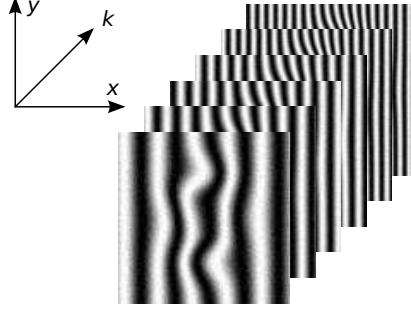


Figure 2: Simulated sequence of fringe images generated varying the fringe frequency.

62 2.2. Frequency detection with the Continuous Wavelet Transform (CWT)

63 Consider a signal as the represented in equation (4), now expressed in a
64 general form as

$$g(k) = g_0(k) + g_1(k) \cos(\phi(k)). \quad (10)$$

65 The Continuous Wavelet Transform of (10) can defined as

$$\mathcal{W}_{a,b}\{g(k)\} = \int_{-\infty}^{\infty} g(k) \psi^* \left(\frac{k-b}{a} \right) dk, \quad (11)$$

66 where ψ represents the mother wavelet and $*$ the complex conjugated. Note
67 that \mathcal{W} is a two-dimensional function of a and b , that represent the scale and
68 shifting, respectively.

69 The choice of a proper form of ψ depends on the particular problem. For the
70 case of a cosine signal as (10), where the parameter to be estimated is the phase
71 or frequency, the most convenient choice is the Gabor wavelet, that in this case
72 can defined as

$$\psi(k) = e^{-\pi k^2} e^{i2\pi f k}, \quad (12)$$

73 which represents a complex periodic function modulated by a gaussian func-
74 tion, where f represents the frequency.

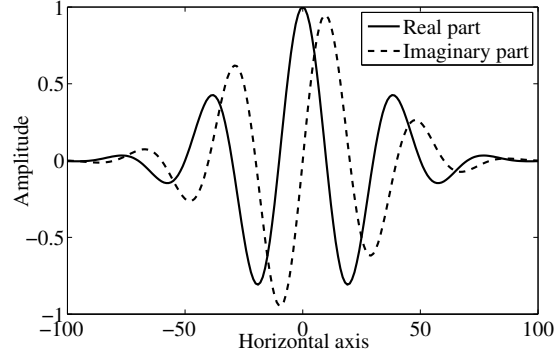


Figure 3: Example of a Gabor wavelet (real and imaginary parts).

75 To explain the process to estimate $\phi(k)$ using the CWT, we rewrite (10) as

$$g(k) = g_0(k) + \frac{g_1(k)}{2}e^{i\phi(k)} + \frac{g_1(k)}{2}e^{-i\phi(k)}. \quad (13)$$

76 Assuming that $g_0(k)$ and $g_1(k)$ are almost constants, then

$$\begin{aligned} \mathcal{W}_{a,b}\{g(k)\} &\approx g_0 \int_{-\infty}^{\infty} e^{-\pi(\frac{k-b}{a})^2} e^{-i2\pi f(\frac{k-b}{a})} dk \\ &+ \frac{g_1}{2} \int_{-\infty}^{\infty} e^{-\pi(\frac{k-b}{a})^2} e^{-i2\pi f(\frac{k-b}{a})} e^{i\phi(k)} dk \\ &+ \frac{g_1}{2} \int_{-\infty}^{\infty} e^{-\pi(\frac{k-b}{a})^2} e^{-i2\pi f(\frac{k-b}{a})} e^{-i\phi(k)} dk. \end{aligned} \quad (14)$$

77 Changing the variables $\nu = f/a$ and $\tau = k - b$, and using the Taylor's series
78 approximation:

$$\phi(\tau + b) \approx \phi(b) + \frac{d\phi(b)}{db}\tau, \quad (15)$$

79 we can approximate $\mathcal{W}_{a,b}\{g(k)\}$ with

$$\begin{aligned}\mathcal{W}_{a,b}\{g(k)\} &\approx g_0 \int_{-\infty}^{\infty} e^{-\pi(\frac{\tau}{a})^2} e^{-i2\pi\nu\tau} d\tau \\ &+ \frac{g_1}{2} e^{i\phi(b)} \int_{-\infty}^{\infty} e^{-\pi(\frac{\tau}{a})^2} e^{i\frac{d\phi(b)}{db}\tau} e^{-i2\pi\nu\tau} d\tau \\ &+ \frac{g_1}{2} e^{-i\phi(b)} \int_{-\infty}^{\infty} e^{-\pi(\frac{\tau}{a})^2} e^{-i\frac{d\phi(b)}{db}\tau} e^{-i2\pi\nu\tau} d\tau.\end{aligned}\quad (16)$$

80 It can be observed in each term of (16) that the factor $e^{-i2\pi\nu\tau}$ represents the
81 Fourier transform kernel, then, evaluating these three Fourier transforms using
82 the modulation and scaling theorems, we obtain

$$\begin{aligned}\mathcal{W}_{a,b}\{g(k)\} &\approx ag_0 e^{-\pi(a\nu)^2} \\ &+ a\frac{g_1}{2} e^{i\phi(b)} e^{-\pi(a\nu - \frac{a}{2\pi} \frac{d\phi(b)}{db})^2} \\ &+ a\frac{g_1}{2} e^{-i\phi(b)} e^{-\pi(a\nu + \frac{a}{2\pi} \frac{d\phi(b)}{db})^2}.\end{aligned}\quad (17)$$

83 Note in (17), that the particular case in which

$$a\nu = \frac{a}{2\pi} \frac{d\phi(b)}{db}, \quad (18)$$

84 gaussian functions in first and third terms are almost zero, while the gaussian
85 function in second term is almost one. At this situation we may call the scaling
86 factor a_r , therefore

$$\mathcal{W}_{a_r,b}\{g(k)\} \approx a_r \frac{g_1}{2} e^{i\phi(b)}. \quad (19)$$

87 Given that for each value of b there is a scaling factor a_r that represents the
88 maximum of \mathcal{W} , it is necessary to detect them to estimate $\phi(b)$. The process
89 to detect a_r is the so called ridge detection. Thus, observing that $\mathcal{W}_{a_r,b}$ is a
90 one-dimensional function we have that

$$W[\phi(k)] = \text{Arg}\{\mathcal{W}_{a_r,b}\{g(k)\}\}, \quad (20)$$

91 where W is the wrapping operator.

As $\phi(k)$ is a linear function, it can be computed from (20) using a simple 1-D unwrapping process. Therefore, the frequency β of a signal like (4) can be estimated from $\phi(k)$ using linear least-squares fitting. Figures (4) and (5) show the process to compute the phase and frequency from $g(k)$.

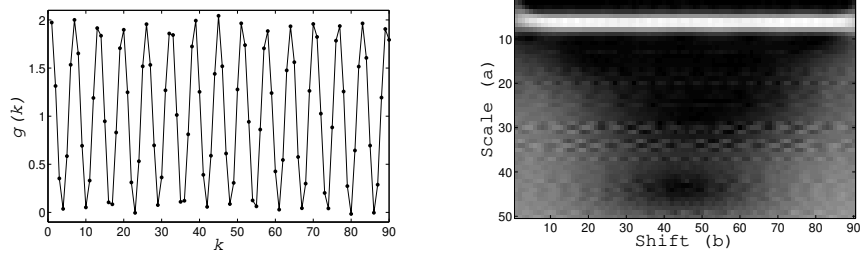


Figure 4: Example of a simulated noisy sinusoidal signal (left) and the magnitude of its Continuous Wavelet Transform (right). Note that the ridge is along the white line of the CWT.

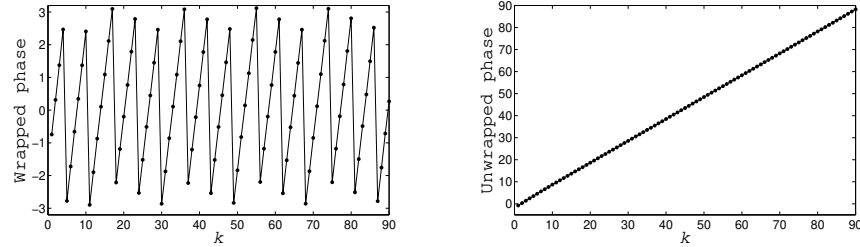


Figure 5: Wrapped and unwrapped phase computed from the signal $g(k)$ represented in Figure (4) using the CWT. The frequency of $g(k)$ is estimated from the unwrapped phase using linear least-squares fitting.

3. Experimental results

3.1. Simulations and error analysis

In this subsection we present some experimental results using the proposed method with simulations. Figure (6) shows a 100×100 simulated depth distribution $Z(x, y)$ using the peaks function included in Matlab. In the same figure we show an image example of the sequence. In this case uniformly distributed

102 phase noise ranging in the interval $[-0.8, 0.8]$ radians was added to each fringe
 103 image. In figure (7) we show the result of the depth distribution and error dis-
 104 tribution obtained using the proposed method. To characterize the performance
 105 of the method we used the Normalized Root Mean Square (NRMS) Error, which
 106 is computed with

$$\text{NRMS-Error} = \sqrt{\frac{\sum (Z - \hat{Z})^2}{\sum Z^2}}, \quad (21)$$

107 where Z and \hat{Z} represent the simulated and recovered depth distribution
 108 respectively. In this experiment the NRMS-error was 0.0113.

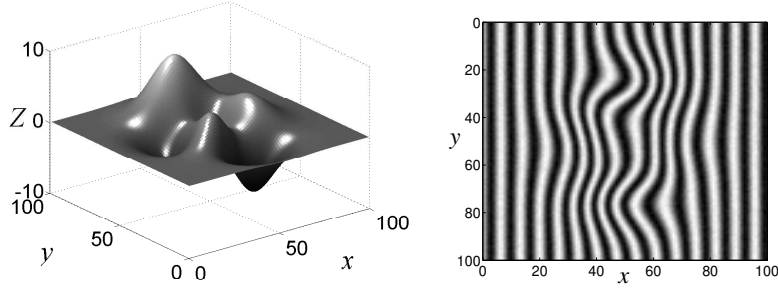


Figure 6: Simulated depth distribution $Z(x, y)$ (left) and an image example of the noisy fringe image sequence with uniformly distributed phase noise (right).

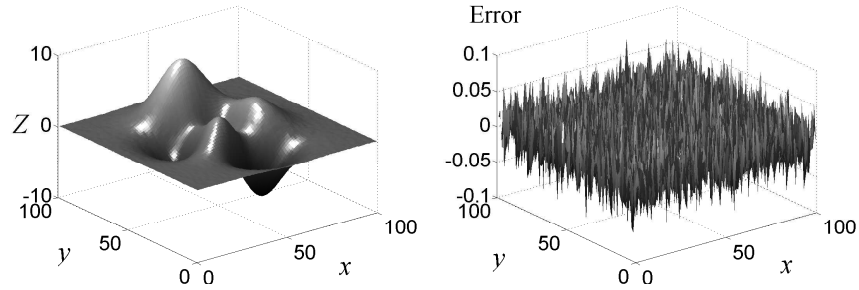


Figure 7: Recovered depth distribution $Z(x, y)$ with the proposed CWT method (left). Error distribution (right).

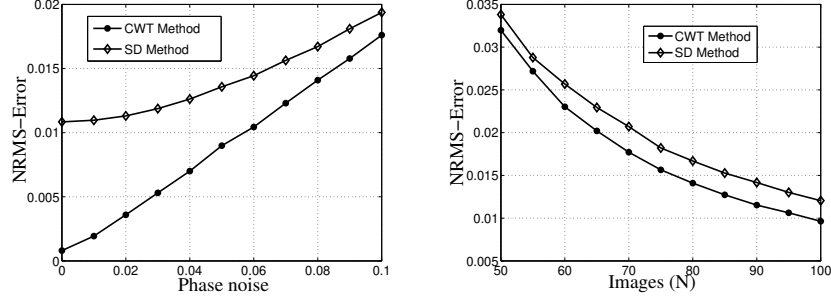


Figure 8: Error analysis using the CWT and the SD adding different values of uniformly distributed phase noise with 80 images (left). Error analysis using the CWT and the SD for different number of images adding phase noise (right).

3.2. Application to real object

In order to experimentally test the proposed method we carried out 3D reconstructions of two real objects. The optical setup used is shown in Figure (1). The CCD camera captures the fringes pattern images projected onto the object. Projected fringes were generated according to equation (4). The μ and x_0 parameters were estimated using the expressions of equation (9) and the objects characteristics.

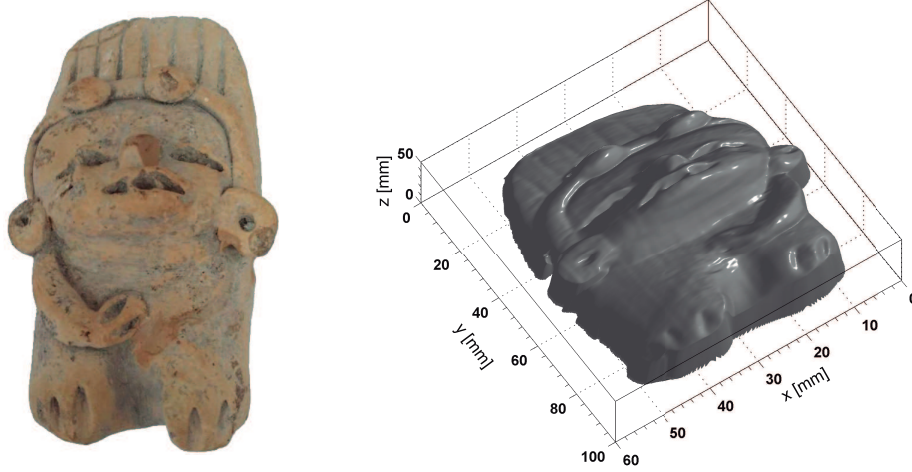


Figure 9: Archaeological vestige. Color image (left) and 3D reconstruction using Wavelet Transform Continuous (right).



Figure 10: Different views of the 3D reconstruction of archaeological piece.

116 The first object is shown in Figure (9). It is an archaeological piece which
 117 corresponding to the indigenous people from Huasteca, Veracruz, Mexico. 3D
 118 information is used for teaching and research as well as the real time and post-
 119 processing archaeological interpretation. These techniques allows to improve of
 120 archaeological studies in depositional and post-depositional contexts [22]. The
 121 setup used to capture vestige was 120 images, $p_0 = 24.6$ mm, $Z_{min} = 0$ mm,
 122 $Z_{max} = 45$ mm, $\Delta\phi_{min} = 0.25\pi$ and $\Delta\phi_{max} = 0.5\pi$. The 3D information
 123 obtained is shown in the Figure (9) and diferents view are shown in the Figure
 124 (10).

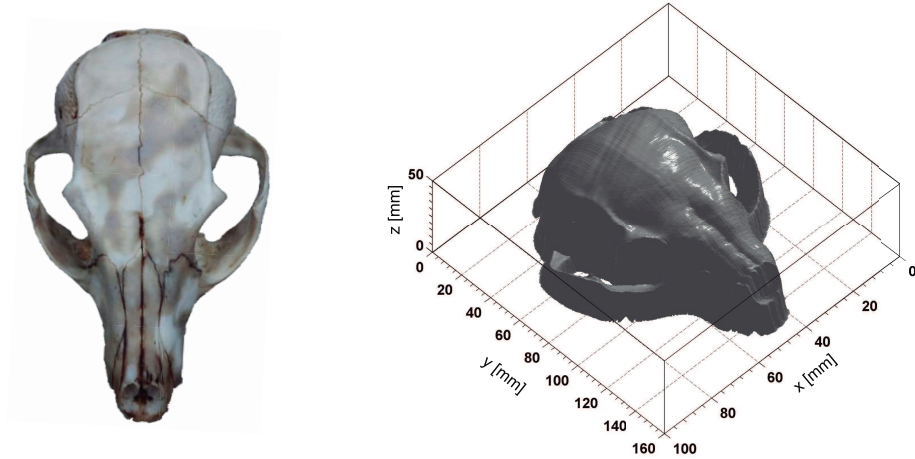


Figure 11: little skull of the families Canidae. Color image (left) and 3D reconstruction using proposed method (right).



Figure 12: Three views of the 3D reconstruction of skull of the families Canidae.

125 The second object, shown in Figure (11), correspond to skull of the fami-
 126 lies Canidae. In geometric morphometrics zoological, 3D reconstruction skull
 127 is used to identify shape differences and help identify the causes of variation
 128 [23]. The setup used to capture of little skull was 120 images, $p_0 = 29.6$ mm,
 129 $Z_{min} = 0$ mm, $Z_{max} = 50$ mm, $\Delta\phi_{min} = 0.25\pi$ and $\Delta\phi_{max} = 0.5\pi$. The 3D
 130 reconstruction obtained is shown in the Figure (11) and three views are shown
 131 in the Figure (12).

132 3.3. Processing time

133 A general purpose laptop with a 2.3 GHz processor and 8 Gb in RAM was
 134 used for capture and processing. Table 1 shows the processing time of the phase
 135 detection using CWT of the simulation performed in section 3.1.

N Images	Processing time (s)
50	0.9619
80	1.1492
100	1.2717
150	1.7119
200	2.112

Table 1: processing time of phase detection for 100x100 simulated depth distribution.

136 The archaeological piece and skull were captured with a CCD point gray
 137 camera (1.3 MP, 1280x960 resolution) and a general purpose projector. Cap-

ture time per image is approximately 0.5 s. Processing time for a setup of 1280x960x80 was 175.114041 s.

4. Conclusions

We have proposed an novel method for the temporal analysis of fringe patterns, based on the Continuous Wavelet Transform. Because the frequency detection is independent in each pixel, the problem of error propagation is solved. This method avoids the complexity of two-dimensional phase unwrapping inherent in spatial methods. The main contribution of this work is frequency detection with CWT of which is obtained the phase as linear function using simple 1-D unwrapping process. The values experimental parameters for a proper sampling are easy tune. These parameters are related to the heights range and the field of vision. Moreover, the method is computationally efficient and processing time so high reasonable.

We have performed a numerical comparison between the CWT and SD techniques. The results obtained show a better accuracy of the CWT, and therefore the number of images can be reduced. On the other hand, the proposed method is more robust to phase noise compared to SD technique. We have also applied the technique to two real object related to zoology and archaeology. 3D profilometry experiment had good results.

5. Acknowledgements

We acknowledge to the Programa para el Desarrollo Profesional Docente (PRODEP) for the partial support of this work and for the posdoctoral grant of Gamaliel Moreno. We also acknowledge to the Consejo Nacional de Ciencia y Tecnología (CONACYT) of México for the scholarship of Gustavo Rodríguez.



Figure 13: Simulated sequence of fringe images generated varying the fringe frequency.

- 162 [1] K. J. Gasvik, *Optical Metrology*, 3rd ed., John Wiley & Sons, (2002).
- 163 [2] G. Cloud, *Optical Methods of Engineering Analysis*, Cambridge University
164 Press, (1995).
- 165 [3] S. Sirohi, *Optical Methods of Measurement, Wholefield Techniques*, Second
166 Edition, CRC Press, (2009).
- 167 [4] R. Leach, *Optical Measurement of Surface Topography*, Springer, (2011).
- 168 [5] S. Zhang, "Recent progresses on real-time 3D shape measurement using
169 digital fringe projection techniques," *Opt. Las. Eng.* **48**(2), 149–158 (2010).
- 170 [6] R. Kulkarni and P. Rastogi, "Optical measurement techniques - A push for
171 digitization," *Opt. Las. Eng.* **87**, 1–17 (2016).
- 172 [7] S. V. Jeught and J. J. J. Dirckx, "Real-time structured light profilometry:
173 a review," *Opt. Las. Eng.* **87**, 18–31 (2016).
- 174 [8] M. Takeda and K. Mutoh "Fourier transform profilometry for the automatic
175 measurement of 3-D object shapes," *Appl. Opt.* **22**(24), 3977–3982 (1983).

- [9] J. Li, X. Y. Su, and L. R. Guo, “Improved Fourier transform profilometry for the automatic measurement of three-dimensional object shapes,” *Opt. Eng.* **29**(12), 1439–1444 (1990).
- [10] D. Malacara, M. Servín and Z. Malacara, *Interferogram Analysis for Optical Testing*, Second Edition, Taylor & Francis (2005).
- [11] D. Li, C. Liu, and J. Tian, “Telecentric 3D profilometry based on phase-shifting fringe projection,” *Opt. Exp.* **22**(26), 31826–31835 (2016).
- [12] L. YePeng, D. Guangliang, Z. ChaoRui, Z. CanLin, S. ShuChun, and L. zhenkun, “An improved two-step phase-shifting profilometry,” *Optik* **127**(1), 288–291 (2016).
- [13] G. A. Ayubi, J. M. Martino, J. R. Alonso, A. Fernandez, C. D. Perciante, J. A. Ferrari, “Three-dimensional profiling with binary fringes using phase-shifting interferometry algorithms,” *Appl. Opt.* **50**(12), 147–154 (2011).
- [14] J. M. Huntley and H. O. Saldner, “Error-reduction methods for shape measurement by temporal phase unwrapping,” *J. Opt. Soc. Am. A* **14**(12), 3188–3196 (1997).
- [15] C. R. Coggrave and J. M. Huntley, “High-speed surface profilometer based on a spatial light modulator and pipeline image processor,” *Opt. Eng.* **38**(9), 1573–1581 (1999).
- [16] T. W. Ng, K T. Ang, and G. Argentini, “Temporal fringe pattern analysis with parallel computing,” *Appl. Opt.* **44**(33), 7125–7129 (2005).
- [17] J. A. Quiroga, J. A. Gomez-Pedrero, “Temporal phase evaluation by Fourier analysis of fringe patterns with spatial carrier,” *J. Mod. Opt.* **48**(14), 2129–2139 (2001).
- [18] J. Villa, J. A. Gomez-Pedrero, J. A. Quiroga, “Synchronous detection technique for temporal fringe pattern analysis,” *Opt. Comm.* **204**, 75–81 (2001).

- 202 [19] C. Zou, L. Huang, M. Zhang, Q. Chen and A. Asundi, “Temporal phase
203 unwrapping algorithms for fringe projection profilometry: A comparative
204 review,” *Opt. Las. Eng.* **85**, 84–103 (2016).
- 205 [20] M. Servin , M. Padilla, G. Garnica, A. Gonzalez, “Profilometry of three-
206 dimensional discontinuous solids by combining two-steps temporal phase
207 unwrapping, co-phased profilometry and phase-shifting interferometry,”
208 *Opt. Las. Eng.* **87**, 75–82 (2016).
- 209 [21] Tomislav Petković, Tomislav Pribanić, Matea Donlić, “Temporal phase un-
210 wrapping using orthographic projection,” *Opt. Las. Eng.* **90**, 34–47 (2017).
- 211 [22] Maurizio Forte “3D Archaeology: New Perspectives and ChallengesThe
212 Example of atalhyk,” *J. E. Mediterr. Archaeol Herit. Stud.* **2**, 1–21 (2014).
- 213 [23] A. Michelle Lawing and P. David Polly “Geometric Morphometrics: Recent
214 Applications to the Study of Evolution and Development,” *J. Zoo.* **280**, 1–7
215 (2009).



